SANDIA REPORT

SAND2000-0827
Unlimited Release
Printed April 2000

Constitutive Models for the Etchegoin Sands, Belridge Diatomite, and Overburden Formations at the Lost Hills Oil Field, California

A. F. Fossum and J. T. Fredrich

Prepared by
Sandia National Laboratories
Albuquerque, New Mexico 87185 and Livermore, California 94550

Sandia is a multiprogram laboratory operated by Sandia Corporation, a Lockheed Martin Company, for the United States Department of Energy under Contract DE-AC04-94AL85000.

Sandia National Laboratories

Issued by Sandia National Laboratories, operated for the United States Department of Energy by Sandia Corporation.

Available to DOE and DOE contractors from
Office of Scientific and Technical Information
P.O. Box 62
Oak Ridge, TN 37831

Prices available from (703) 605-6000
Web site: http://www.ntis.gov/ordering.htm

Available to the public from
National Technical Information Service
U.S. Department of Commerce
5285 Port Royal Rd
Springfield, VA 22161

DISCLAIMER

Portions of this document may be illegible in electronic image products. Images are produced from the best available original document.

SAND2000-0827
Unlimited Release
Printed April 2000

Constitutive Models for the Etchegoin Sands, Belridge Diatomite, and Overburden Formations at the Lost Hills Oil Field, California

A. F. Fossum
Materials Mechanics Department

J. T. Fredrich
Geophysical Technology Department

Sandia National Laboratories
P.O. Box 5800
Albuquerque, NM 87185-0750

Abstract

This report documents the development of constitutive material models for the overburden formations, reservoir formations, and underlying strata at the Lost Hills oil field located about 45 miles northwest of Bakersfield in Kern County, California. Triaxial rock mechanics tests were performed on specimens prepared from cores recovered from the Lost Hills field, and included measurements of axial and radial stresses and strains under different load paths. The tested intervals comprise diatomaceous sands of the Etchegoin Formation and several diatomite types of the Belridge Diatomite Member of the Monterey Formation, including cycles both above and below the diagenetic phase boundary between opal-A and opal-CT. The laboratory data are used to derive constitutive parameters for the Extended Sandler-Rubin (ESR) cap model that is implemented in Sandia's structural mechanics finite element code JAS3D. Available data in the literature are also used to derive ESR shear failure parameters for overburden formations. The material models are being used in large-scale three-dimensional geomechanical simulations of the reservoir behavior during primary and secondary recovery.

This page intentionally left blank.

Acknowledgements

This work was performed under sponsorship of the U.S. Department of Energy's Natural Gas and Oil Technology Partnership, National Petroleum Technology Office. Additional funding was provided by two independent Work For Others Funds-In Agreements with Aera Energy LLC and Chevron USA Production Co. Chevron and Aera Energy also sponsored the laboratory testing program that was performed by TerraTek, Inc. and that provided the experimental rock mechanics data that are used in this work. The DOE National Petroleum Technology Office sponsored publication of this report.

Tony Murer (Aera Energy LLC), Russ Ewy (Chevron Petroleum Tech. Co.), and Greg Mazmanian and Rick Caprio (both Chevron USA Prod. Co.) contributed useful information and data related to the reservoir and overburden geology at Lost Hills. This data served to guide some aspects of the material model development. Larry Myer (Lawrence Berkeley Laboratory) and Mike Bruno (Terralog Technologies) contributed extensively to the analyses of field data that motivated the work reported here.

The work that is described in this report has been performed as part of a larger collaborative National Laboratory/Industry project between Sandia National Laboratories, Lawrence Berkeley National Laboratory, Terralog Technologies, Aera Energy LLC, Bakersfield Energy Resources, Chevron Petr. Tech. Co., Chevron USA Prod. Co., Crutcher-Tufts Prod. Co., HarCor Energy, Shell E&P Tech. Co., and Texaco E&P Inc.

This page intentionally left blank.

Table of Contents

This page intentionally left blank.

Figures

Tables

This page intentionally left blank.

1 Introduction

In 1994 a cooperative National Laboratory/industry research program was initiated to improve understanding of the geomechanical processes causing well casing damage during oil production from weak, compactable formations. The study focuses on the shallow diatomaceous oil reservoirs located in Kern County, California, and combines analyses of historical field data, experimental measurement of rock mechanical behavior, and development of geomechanical models to simulate the reservoir and overburden response to production and injection during primary and secondary recovery.

A comprehensive database, consisting of historical well failure, production, injection, and subsidence data was compiled to provide unique, complete pictures of the diatomite reservoirs and overburden behavior at both the Belridge (*Myer et al.*, 1996, *Fredrich et al.*, 1996) and Lost Hills fields situated in the San Joaquin basin. Thorough analysis of the database for Belridge indicated that two-dimensional (plane-strain) geomechanical simulations could not capture the locally complex production, injection, and subsidence patterns, and motivated large-scale, three-dimensional geomechanical simulations. Central to the numerical modeling work has been the use of sophisticated material models that capture accurately the highly non-linear deformation behavior of the reservoir rock, including inelastic compaction (yield) at stress states below the shear failure surface.

Fredrich et al. (1996, 1998, 2000) described the development of three-dimensional geomechanical models for the Belridge field and the historical simulations that were performed collaboratively with Shell E&P Technology Co. and Aera Energy LLC for Sections 33 and 29 using Sandia National Laboratories' quasi-static large-deformation structural mechanics finite element code, JAS3D (*Blanford et al.*, 1996). JAS3D provides several constitutive models to simulate time-independent elastic and inelastic (non-linear) deformation as well as time-dependent (creep) behavior. One of these material models, referred to as the Extended Sandler-Rubin (ESR) cap model (*Fossum et al.*, 2000), is a generalized version of the Sandler and Rubin cap plasticity model (*Sandler and Rubin*, 1979). The ESR cap model includes a non-linear shear failure surface and a second yield surface (cap) to account for inelastic compaction at stress states lower than those required to induce shear failure. *Fossum and Fredrich* (1998) described the development of cap plasticity models for several cycles of the Belridge Diatomite at the Belridge field in California.

The historical simulations for the Belridge field served to validate the conceptual model that was formulated for casing damage and the geomechanical modeling approaches. This work also demonstrated that geomechanical simulation can be applied as a reservoir management tool to optimize production and injection policies for existing field developments, and to identify the most economical strategy for infill drilling, such as the relative density and placement of production and injection wells.

Following the successful application at Belridge, attention shifted to the Lost Hills oil field. The Lost Hills field is at an earlier stage of development than the Belridge field, and therefore, development and application of geomechanical models for the Lost Hills field

were expected to be particularly useful in regard to infill drilling and expansion of the waterflood.

This report documents the development of material models for the Lost Hills oil field. Constitutive parameters for the ESR cap model were derived from experimental rock mechanics test data for the two reservoir formations (including two diatomaceous sand units of the Etchegoin Formation and three cycles of the Belridge Diatomite Member of the Monterey Formation). Shear failure parameters for the ESR model were also derived for the strata underlying the reservoir (Opal CT diatomite). Existing data in the literature were used to determine shear failure parameters for the ESR model for the overburden formations, including the San Joaquin Formation, Tulare Formation, and alluvium.

2 Geology, Stratigraphy, and Lithology at Lost Hills

The Lost Hills oil field is one of several significant oil fields located in the San Joaquin basin of central California (*Graham and Williams*, 1985). Other major fields include Belridge, Cymric, Elk Hills, Buena Vista, and Midway-Sunset. The Lost Hills field is about 45 miles northwest of Bakersfield in Kern County, and the producing structure is a northwest-southeast trending doubly-plunging anticline that roughly parallels the San Andreas fault about 25 miles to the west. The anticline is about one mile wide and 12 miles long and slightly asymmetric, with dips approaching ~20° on the eastern flank as compared to ~10° on the western flank. *Stewart et al.* (1994) estimated about 2 billion bbl of oil-in-place. The structural setting is similar to that of the Belridge and Cymric fields directly to the south.

The main reservoir is relatively shallow and the producing intervals reach a maximum thickness of approximately 1500 feet along the crest, and thin on the flanks. A generalized stratigraphic column for the Lost Hills area is shown in Figure 2.1. Most production is from the Belridge Diatomite Unit of the Reef Ridge Member of the Upper Miocene Monterey Formation. Overlying the Belridge Diatomite are partially saturated sands of the Etchegoin Formation, the Pliocene San Joaquin Formation, and the Pleistocene Tulare Formation. The overburden formations generally thin from the flanks to the crest, reaching a total thickness of about ~1000 feet along the crest. Reservoir production extends up through the C and D sands of the late Pliocene to early Miocene Upper Etchegoin Formation that overlie unconformably the Reef Ridge Member, as well as down into the uppermost interval of the Brown Shale Member of the Monterey Formation. Underlying the Brown Shale are the McLure and Devilwater Members of the Monterey Formation.

Diatomite is a biogenic siliceous deposit consisting of the shells or tests of diatoms with varying amounts of detrital material (principally clay and sand) so that individual depositional cycles are identifiable, with the rock ranging from fairly pure to shaley diatomite. In the upper intervals, diatoms are preserved as opal-A, which is an amorphous, colloidal form of silica, and porosity of the Belridge diatomite unit ranges typically from 50-60% at Lost Hills. With increasing depth (pressure) and temperature, the mineralogic phase changes from opal-A to opal-CT. The associated reduction in porosity (<45%) makes the

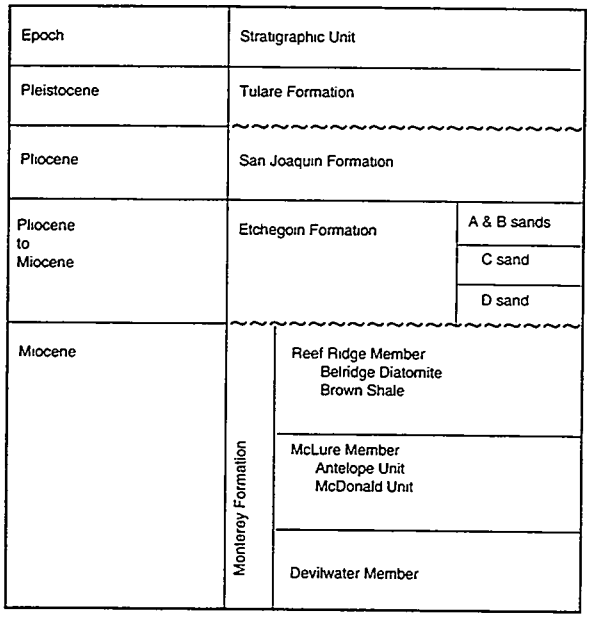

Figure 2.1 Generalized stratigraphic column, Lost Hills Field.

diatomite less productive below the opal-CT transition, and most production at Lost Hills is from the opal-A phase of the Belridge Diatomite Unit. Below this, the diatom skeletal structures are no longer well preserved and the rock is termed a porcelanite. The opal A/CT transition is tilted across the field, and occurs at a slightly shallower depth on the western versus eastern flank. Because of the asymmetric structure, in some places the Belridge Diatomite is entirely in the opal-A phase, with the transition to opal-CT occurring beneath in the Brown Shale Member. With further depth, the opal-CT phase is replaced by chert.

The main producing formation at the Lost Hills field is stratigraphically equivalent to the Belridge Diatomite unit that is one of two reservoir formations at the Belridge field located to the south. However, because of its relative position with respect to sources of terrigenous clastic sediments during deposition, the Belridge Diatomite at Lost Hills is less pure than at Belridge. Also, the unit is thicker and shallower at Belridge than at Lost Hills.

Because of the lower purity and more variable composition of the diatomite at Lost Hills, a compositional scheme is used to characterize the diatomite. The two primary operators at Lost Hills, Aera Energy LLC and Chevron USA Prod. Co., identify three type diatomites that correspond to compositional variations. Neutron density logs are used to classify the rock types with depth as indicated in Table 2.1.

Table 2.1 Composition and Physical Properties of Diatomite, Lost Hills Field (*Fast et al.* 1992, 1993).

Type	Approximate Composition (%)			Bulk Density (g/cc)	Approximate Porosity (%)	Approximate Bench Permeability (mDa)
	Diatomite	Clays	Silt			
1	~ 60	~ 20	~ 20	<1.6	60	1.4
2	~ 40	~ 40	~ 20	1.6- 1.75	55	1.2
3	~ 25	~ 25	~ 50	>1.75	50	3.0

3 Description of the ESR Cap Plasticity Model

The ESR cap model is a generalization of the soil and rock constitutive model of *Sandler and Rubin* (1979). The model is designed to represent the elastic-plastic behavior of porous rock and soil. The yield surface comprises a nonlinear, non-hardening shear yield surface and a hardening or softening cap surface each of which can vary with Lode angle (as defined later). This composite shear-failure/yield-cap surface is illustrated in Figure 3.1. The dashed line in Figure 3.1 depicts a triaxial compression load path. Linear elastic behavior occurs when the stress point is within the composite shear-failure and yield-cap surfaces. For the load path and the initial yield surface shown in Figure 3.1, the material compacts after intersecting the initial yield surface and compaction hardens (i.e., pushes the cap out) until the stress point reaches the shear-failure surface at which point the material fails in shear.

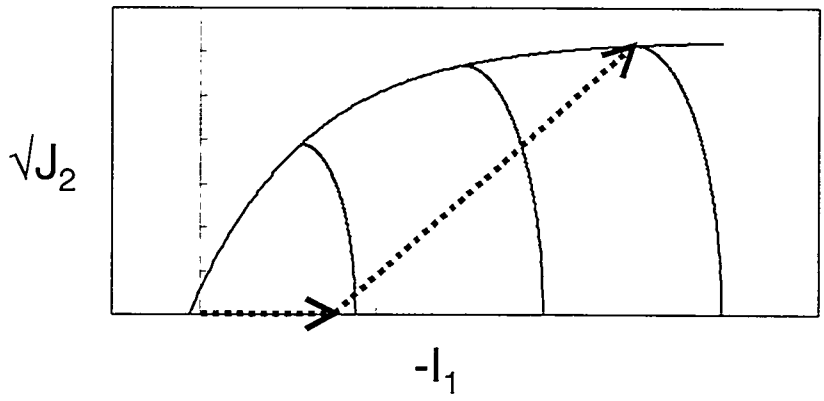

Figure 3.1 Shear and cap yield surfaces depicted with a triaxial compression load path. I_1 is the mean stress and $\sqrt{J_2}$ is the square root of the second invariant of the deviatoric stress.

It is assumed that the elastic strain is always much less than unity, so that the strain-rate measure can be decomposed into the sum of an elastic component and an inelastic component as

$$\dot{\varepsilon}_{ij} = \dot{\varepsilon}^e_{ij} + \dot{\varepsilon}^p_{ij} . \tag{3.1}$$

The stresses can be determined from Hooke's Law and Eq. 3.1 as

$$\dot{\sigma}_{ij} = C_{ijkl}\left(\dot{\varepsilon}_{kl} - \dot{\varepsilon}^p_{kl}\right) \tag{3.2}$$

where the fourth-order elastic coefficient matrix, C_{ijkl}, is given in terms of the shear modulus, G, and bulk modulus, K, as

$$C_{ijkl} = 2G\delta_{ik}\delta_{jl} + \left(K - \frac{2}{3}G\right)\delta_{ij}\delta_{kl} . \tag{3.3}$$

When the stress point lies on the shear-failure envelope, shear failure occurs according to the yield function, F_S,

$$F_s = \Gamma\sqrt{J_2} - A + C\exp(BI_1) \tag{3.4}$$

where J_2 is the second invariant of the deviator stress; I_1 is the first invariant of the Cauchy stress; and A, B, and C are material constants. The Γ is a function of J_3, the third invariant of the deviator stress that incorporates the Lode-angle dependence of yield, given by

$$\Gamma = \frac{1}{2}\left\{[1+\sin(3\Psi)] + \frac{1}{K}[1-\sin(3\Psi)]\right\} \tag{3.5}$$

where K is the ratio of the yield stress in triaxial extension to the yield stress in triaxial compression and Ψ is the Lode angle given by

$$\Psi = \frac{1}{3}\text{asin}\left(-\frac{27}{2}\frac{J_3}{(3J_2)^{3/2}}\right) \quad -\frac{\pi}{6} \le \Psi \le \frac{\pi}{6}. \tag{3.6}$$

For triaxial extension, $\Psi = -\pi/6$, and for triaxial compression, $\Psi = \pi/6$. In the case of triaxial compression, $\Gamma = 1$, while $\Gamma = 1/K$ for triaxial extension. Thus, in this formulation the difference in strength between triaxial compression and triaxial extension stress states is handled by multiplying the loading variable, $\sqrt{J_2}$ by a factor Γ such that the yield function experiences an apparent higher loading condition for stress states different from triaxial compression, depending on the value of J_3.

When the stress point lies on the cap and pushes it outward, plastic strain causes an irreversible decrease in volume called compaction, and a shear component for stress states other than pure hydrostatic compression. The cap motion is related to the plastic decrease in volume through a hardening rule. The elliptical shape of the cap is defined through the cap yield function,

$$F_c = \Gamma\sqrt{J_2} - \frac{1}{R}\sqrt{(X-L)^2 - (I_1-L)^2} \tag{3.7}$$

in which L is the value of I_1, at which the cap intersects the shear surface, and

$$X(L) = L - R[A - C\exp(BL)]. \tag{3.8}$$

The material parameter, R defines the ratio of principal ellipse radii of the cap surface. The cap intersects the shear failure surface at the point on the cap with zero horizontal tangency, i.e., the point of zero dilatancy. When the cap is too small to intersect the shear failure surface, a von Mises surface extends from the point of horizontal tangency to either the shear failure or tension cut-off surface.

The plastic strain rates, $\dot{\varepsilon}_{ij}^{p}$, can be determined from a flow rule,

$$\dot{\varepsilon}_{ij}^{p} = \dot{\gamma}\frac{\partial F}{\partial \sigma_{ij}} \tag{3.9}$$

if $F(\sigma_{ij}, L)$ is constructed to be the composite yield function defined as the union of the shear and cap yield functions, $F = F_s \bigcup F_c$ and where $\dot{\gamma}$ is the consistency parameter. Since subsequent loading surfaces pass through the loading point, the yield function, F, is such that

$$F(\sigma_{ij}, L) = 0 \tag{3.10}$$

where the state variable L is governed by an evolution equation of the form

$$\dot{L} = \dot{\gamma} h_L(\sigma_{ij}, L) \tag{3.11}$$

where h_L is a hardening function. During loading, the consistency condition (Eq. 3.10), requires that

$$\dot{F} = \frac{\partial F}{\partial \sigma_{ij}}\dot{\sigma}_{ij} + \frac{\partial F}{\partial L}\dot{L} = 0. \tag{3.12}$$

From Eqs. 3.2, 3.9, 3.11, and 3.12, the consistency parameter, $\dot{\gamma}$, can be determined from

$$\dot{\gamma} = \frac{\dfrac{\partial F}{\partial \sigma_{ij}} C_{ijkl}\dot{\varepsilon}_{kl}}{\dfrac{\partial F}{\partial \sigma_{ij}} C_{ijkl}\dfrac{\partial F}{\partial \sigma_{kl}} - \dfrac{\partial F}{\partial L}h_L}. \tag{3.13}$$

The hardening parameter is determined as follows. In incremental form, the trace of Equation 3.9 gives the incremental plastic volume strain as

$$\Delta\varepsilon_{kk}^{p} = \Delta\varepsilon_{V}^{p} = 3\Delta\gamma\frac{\partial F}{\partial I_1}. \tag{3.14}$$

Now, by specifying an isotropic hardening rule in the form of a pressure-volume relation,

$$\varepsilon_{v}^{p} = W\left|\exp\left\{D_1(X - X_0) - D_2(X - X_0)^2\right\} - 1\right| \tag{3.15}$$

in which W, D_1 and D_2 are material parameters and X_0 is the initial cap position, one can obtain another expression for the incremental plastic volume strain as

$$\Delta\varepsilon_{V}^{p} = \frac{\partial \varepsilon_{V}^{p}}{\partial X}\frac{\partial X}{\partial L}\Delta L \tag{3.16}$$

where

$$\frac{\partial \varepsilon_V^p}{\partial X} = W[D_1 - 2D_2(X - X_0)]\exp\{D_1(X - X_0)\}\exp\{-D_2(X - X_0)^2\} \tag{3.17}$$

and

$$\frac{\partial X}{\partial L} = 1 + RBC\exp(BL) \qquad L < L_0 . \tag{3.18}$$

Thus, from Eqs. 3.14 and 3.16 an expression for ΔL can be found as

$$\Delta L = \frac{3\Delta\gamma \dfrac{\partial F}{\partial I_1}}{\dfrac{\partial \varepsilon_V^p}{\partial X}\dfrac{\partial X}{\partial L}} . \tag{3.19}$$

Since the incremental form of Eq. 3.11 is given by

$$\Delta L = \Delta\gamma h_L \tag{3.20}$$

the cap hardening function, h_L, can be found from Eqs. 3.19 and 3.20 as

$$h_L = \frac{3\dfrac{\partial F}{\partial I_1}}{\dfrac{\partial \varepsilon_V^p}{\partial X}\dfrac{\partial X}{\partial L}} . \tag{3.21}$$

The formulation of the ESR cap plasticity model in terms of classical plasticity concepts is thus complete.

4 Development of Constitutive Models for Lost Hills

The geomechanical simulation effort required the development of a suite of material models to simulate the response of the reservoir and overburden formations to pore pressure changes caused by primary production (drawdown) and secondary recovery (drawdown at production wells and pressure maintenance at injection wells). The simulations also required development of a material model to represent the rock formations underlying the reservoir (underburden). The produced reservoir formations are subjected to changes in pore pressure that lead to compaction, whereas the overburden units are subjected to stress changes as a result of deformations of the underlying reservoir formations.

4.1 Geomechanical Units

ESR cap model parameters were derived for five distinct rock types representing the reservoir formations (Table 4.2). In accord with the customary practices of the field

operators (Table 2.1), three intervals of opal-A Belridge Diatomite representing Type 1 ("clean"), Type 2 ("shaley"), and Type 3 ("sandy") diatomite were characterized. In addition, the two sand units of the overlying Etchegoin Formation that are also produced at Lost Hills (C and D sands) were characterized. Finally, to represent the porcelanite rock that lies below the production horizon, core samples of the Belridge Diatomite member obtained from a depth below the opal A/CT transition (Table 4.2) were tested to derive shear failure parameters for the ESR cap model.

Material models for the remaining overburden formations were developed using data available from the literature since no core was available (Table 4.2). Mohr envelope failure data for the San Joaquin Formation determined from rock mechanics tests on cores from the Lost Hills field (*Bruno and Bovberg*, 1992) were used to determine shear failure parameters for the ESR cap model. The Drucker-Prager constitutive parameters applied by *Fredrich et al.* (1996) to the Tulare Formation at the Belridge field were used to calculate equivalent shear failure parameters for the ESR cap model. Likewise, Drucker-Prager parameters for the alluvium used in the prior Belridge work were similarly applied.

Table 4.1 Core samples and other data used for development of material models for the Lost Hills Field

Section of Geomechanics Model	Geological unit		Well	Depth (feet)	Comments
Overburden	Alluvium		No core available	N/A	DP parameters used from prior Belridge study
	Tulare Formation		No core available	N/A	DP parameters used from prior Belridge study
	San Joaquin Formation		Chevron, Sect. 7, well Cahn 7-7D	1399 – 1412	Mohr envelope failure data from *Bruno & Bovberg* (1992)
	Etchegoin Formation– A & B sands		No core available	N/A	
Reservoir	Etchegoin Formation	C sand	Aera Energy, Lost Hills 1, well #485	1498	Diatomaceous sand
		D sand	Aera Energy, Lost Hills 1, well #485	1628	Diatomaceous sand
	Belridge Diatomite Member (Opal A)	E	Chevron, Sect. 32, well OB-4A	1483.0– 1484.0	Type 1 Diatomite
		EE	Chevron, Sect. 32, well OB-4A	1527.3– 1533.7	Type 3 Diatomite
		G	Chevron, Sect. 32, well OB-4A	1655.6– 1666.0	Type 2 Diatomite
Underburden	Belridge Diatomite Member (Opal CT)		Chevron, Sect. 9, well 9-14F	2631 & 2658	Porcelanite

4.2 Laboratory Rock Mechanics Tests

Triaxial rock mechanics tests were conducted on samples prepared from cores recovered from both the Etchegoin Formation and Belridge Diatomite unit at the Lost Hills field (see Table 4.1). The tests were conducted by TerraTek, Inc., and designed to provide axial and radial stress (σ) and strain (ε) data under a variety of load paths. The three load paths used in the laboratory program included hydrostatic compression (loading with $\sigma_1=\sigma_2=\sigma_3$), uniaxial strain (axial stress σ_1 loading with radial stresses $\sigma_2=\sigma_3$ increased as

required to maintain radial strain $\varepsilon_2=\varepsilon_3=0$), and conventional triaxial compression (hydrostatic loading followed by increasing σ_1 with $\sigma_2=\sigma_3$=constant).

The cylindrical test samples were prepared perpendicular to bedding (i.e. vertically oriented cores), with diameter to length dimension of either 1×2 inches or 1.5×3 inches. Samples were jacketed to prevent the confining fluid from penetrating the samples and tested in a servo-controlled triaxial system with the pore pressure system drained to the atmosphere. Confining pressure was measured with a conventional strain gauge transducer, and measurements of force on an internal load cell were used to calculate axial stress. Axial and radial strains were measured using cantilever-type strain transducers, with corrections applied for elastic distortion of the end-caps and jacketing material. Radial deformations were measured at two perpendicular directions along the sample mid-point, and averaged for calculating radial strain. Load-unload cycles (with typical excursions of 300 psi) were performed during at least two tests on each rock type to enable determination of elastic moduli.

4.3 Parameter Estimation

4.3.1 Elastic Parameters

Since isotropic elasticity is assumed it suffices to measure any two elastic constants. In the current study, the shear modulus, G, and Young's modulus, E, were determined from the unload-reload portions of conventional triaxial compression tests, while G and the bulk modulus, K, were determined from the unload-reload portions of uniaxial strain tests. The authors judiciously selected the ranges of the unload-reload stress-strain curves from which to evaluate these moduli. To calculate a shear modulus from triaxial compression tests, the axial stress minus radial stress is plotted versus the axial strain minus radial strain for the selected part of the unload-reload portion of the test. The slope is equal to twice the shear modulus. If the same stress difference is plotted versus the axial strain, the slope is equal to the Young's modulus. The bulk modulus can then be determined in terms of the shear and Young's moduli as

$$K = \frac{GE}{3(3G - E)}. \tag{4.1}$$

For uniaxial strain tests, the slope of the unload-reload portion of the axial minus radial stress versus axial strain is similarly equal to $2G$. The slope of the unload-reload portion of the mean stress versus axial strain plot is equal to the bulk modulus.

4.3.2 Shear Failure Parameters

A suite of triaxial compression tests, each conducted at a different confining pressure, is used to determine the parameters A, B, and C appearing in Eq. 3.4. The peak value of $\sqrt{J_2}$ is determined for each test from a $\sqrt{J_2}$ versus I_1 plot. These values of $\sqrt{J_2}$

together with their corresponding I_1 values are then assembled as data pairs into a fitting database. Nonlinear regression is used to determine a set of material parameter estimates in the sense of least squares. A merit function is minimized to determine best-fit parameters. It is assumed that the measurement error is normally distributed with a mean of zero. An appropriate merit, or objective function, is the weighted sum of squared residuals given by

$$\Phi(P) = \sum_{i=1}^{N} w_i [y_i - y(x_i; P)]^2 \qquad (no\ sum\ on\ repeated\ i) \tag{4.2}$$

where $y(x_i; P)$ represents the model dependent-variable response prediction at the ith of N data points; y_i is the ith dependent variable data point value; x_i is the ith independent variable data point value; P is the vector of parameters to be estimated; and w_i is the weight factor. In the current application, I_1 is chosen as the independent variable and $\sqrt{J_2}$ as the dependent variable, i.e.,

$$y(x_i; P) = \sqrt{J_2} = A - C\exp(BI_1). \tag{4.3}$$

The weight factors, w_i, were chosen arbitrarily as $w_i = 1/y_i$.

4.3.3 Cap Parameters

Once the elastic and shear failure parameters have been established, they are held fixed while the cap parameters are determined through nonlinear regression involving direct simulation of the triaxial tests (either uniaxial strain or conventional triaxial compression) using the procedure described above. The principal laboratory-measured strains were used as the independent variable values while axial stress was used as the dependent variable. Eqs. 3.2 through 3.21 were solved numerically to determine the dependent variable, axial stress, as a function of the independent variables, axial and radial strains. The parameters were determined from an iterative application of the Levenberg-Marquardt optimization method as described by *Fossum* (1997), but using numerical derivatives for the Hessian matrix.

4.4 Constitutive Parameters

4.4.1 Belridge Diatomite Unit – Type 1 (Clean) Diatomite

Table 4.2 identifies the tests and specimens used in the estimation of material parameters for the Type 1 Diatomite. All test specimens were prepared from cores that were preserved. Tests Lhls_1b (50 psi) and Lhls_5b (200 psi) clearly reached a peak stress difference while test Lhls_4Ab (500 psi) appeared to be very close to reaching a peak stress difference. Test Lhls_6b (1000 psi) did not appear to have reached a peak stress difference and was therefore not used to determine shear failure parameters. Figure 4.1 shows the model fit to the shear failure data along with the shear failure parameters. Note that even

though test Lhls_6b was not used in the fitting routine, the model predicts failure at the maximum stress difference reached in test Lhls_6b (depicted as an open triangle in Figure 4.1). Thus, the maximum stress difference observed in this test was indeed possibly close to maximum. Cap model parameters were determined using the two uniaxial strain tests and the triaxial compression test conducted at 50 psi confining pressure. Figure 4.2 shows the model fit to these data along with the best-fit parameters. The triaxial compression tests at 200, 500, and 1000 psi included extended hold periods that precluded use of that data due to the time independence of the material model. "Zeroing out" the strains during the hold period is not possible because commensurate with the strains during the hold period is cap hardening. Because the cap hardening affects the cap behavior upon resumption of the triaxial loading the hold period cannot be simply zeroed out.

Table 4.2 Type 1 Diatomite test information and derived elastic properties

Test No.	Sample ID	Depth (ft.)	Bulk Density (g/cm^3)	Load Path	2x Shear Modulus (psi)	Bulk Modulus (psi)
Lhls_1b	1-1	1,483	1.611	Triaxial Compression (50 psi)	No Unload	No Unload
Lhls_5b	5-3	1,484	1.612	Triaxial Compression (200 psi)	62,818	43,632
Lhls_4ab	4-2	1,483.5	1.594	Triaxial Compression (500 psi)	No Unload	No Unload
Lhls_6b	6-3	1,484	1.553	Triaxial Compression (1000 psi)	108,392	320,250
Chv2a-2	2A	1483.5	1.573	Uniaxial Strain	64,399	44,031
Chv2b-1	2B	1483.5	1.534	Uniaxial Strain	48,139	35,208

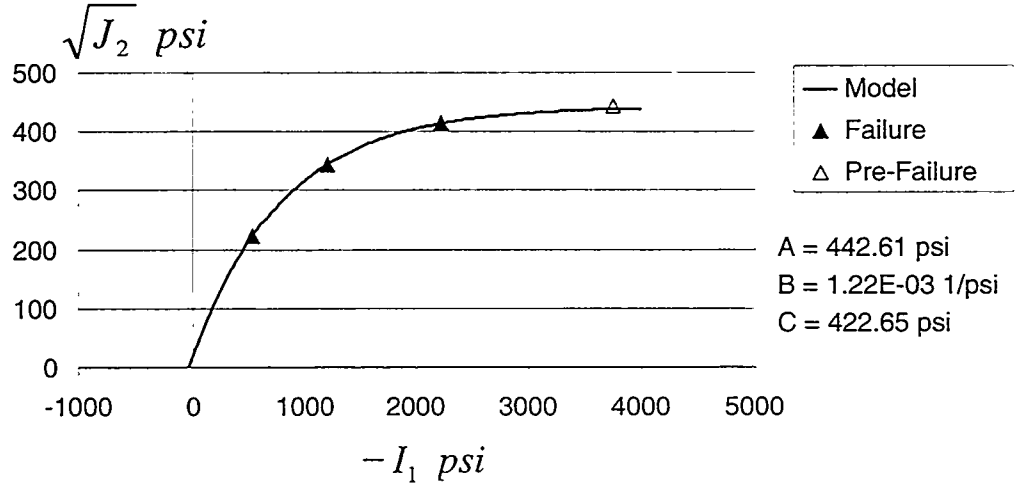

Figure 4.1 Shear failure model fit to conventional triaxial compression test data for Type 1 Diatomite (see Table 4.2)

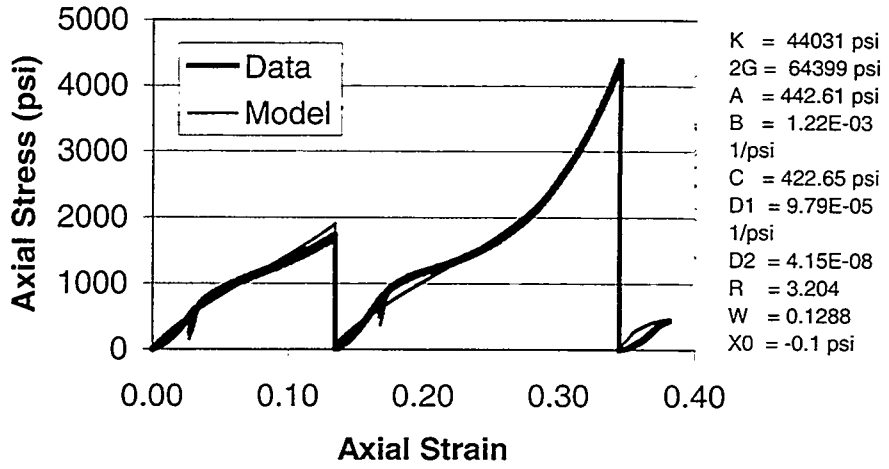

Figure 4.2 Measured versus predicted axial stress – axial strain behavior for two uniaxial strain tests (first two tests shown), and for a triaxial compression test at 50 psi (third shown) for Type 1 Diatomite (see Table 4.1). Note that the hydrostatic load segment of the triaxial test is included.

4.4.2 Belridge Diatomite Unit – Type 3 (Sandy) Diatomite

Table 4.3 identifies the tests and specimens used in the estimation of material parameters for Type 3 Diatomite. All test specimens were prepared from cores that were not preserved. Tests Lhls_25b (50 psi) and Lhls_26b (200 psi) clearly reached a peak stress difference while test Lhls_18b (500 psi) appeared to be close to reaching a peak stress difference. Thus these three tests were used to determine the shear failure parameters. Figure 4.3 shows the model fit to the shear failure data as well as the shear failure parameters. The two uniaxial strain tests, in addition to three triaxial compression tests (at 50, 200, and 500 psi) were used for determination of the remaining cap plasticity parameters. Figure 4.4 shows the model fit to these data along with the best-fit parameters. The triaxial compression test at 1000 psi could not be used because of the protracted hold period following the hydrostatic loading. As discussed previously, the time independence of the material model precludes the occurrence of creep deformation.

Table 4.3 Type 3 Diatomite test information and derived elastic properties

Test No.	Sample ID	Depth (ft.)	Bulk Density (g/cm^3)	Load Path	2 x Shear Modulus (psi)	Bulk Modulus (psi)
Lhls_25b	25-1D	1,533.7	1.734	Triaxial Compression (50 psi)	No unload	No unload
Lhls_26b	26-1D	1,533.7	1.773	Triaxial Compression (200 psi)	118,863	71,130
Lhls_18b	18-1D	1,533.7	1.735	Triaxial Compression (500 psi)	No unload	No unload
Lhls_21b	21-1D3	1,527.3	1.711	Triaxial Compression (1000 psi)	152,986	322,347
Chv1d2-1	1D2	1,529.4	1.681	Uniaxial Strain	110,909	88,961
Chv1d7-1	1D7	1,530.5	1.748	Uniaxial Strain	99,708	77,745

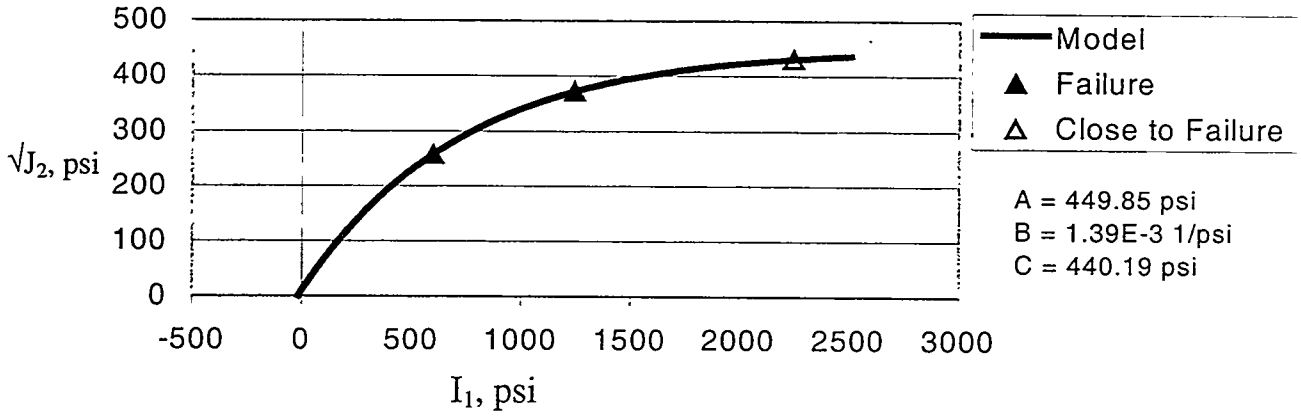

Figure 4.3 Shear failure model fit to conventional triaxial compression test data for Type 3 Diatomite (see Table 4.3)

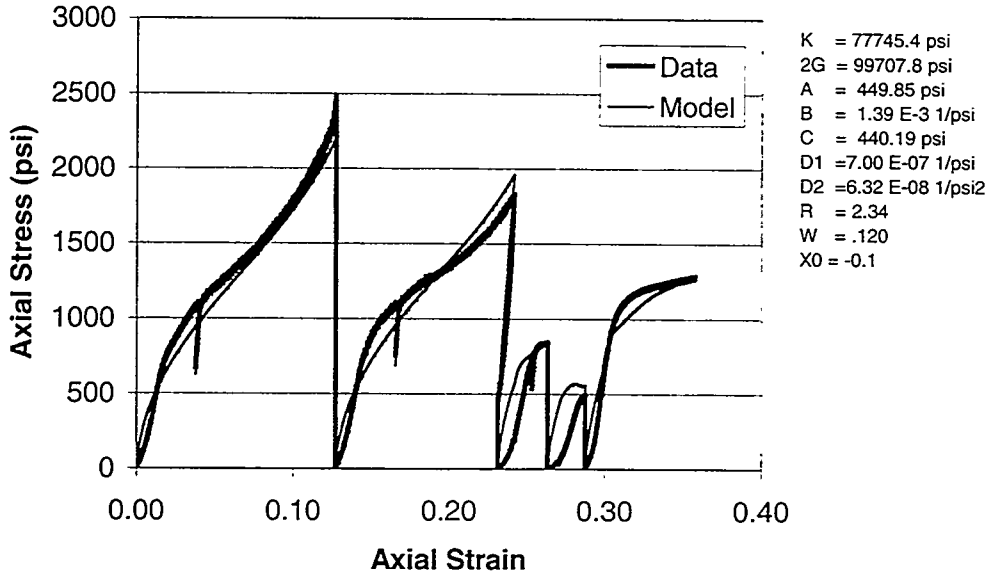

Figure 4.4 Measured versus predicted axial stress – axial strain behavior for two uniaxial strain tests (first two tests shown) and three triaxial compression tests at 50, 200, and 500 psi (third through fifth shown) for Type 3 Diatomite (see Table 4.3). Note that the hydrostatic load segments of the triaxial tests are included.

4.4.3 Belridge Diatomite Unit – Type 2 (Shaley) Diatomite

Table 4.4 identifies the test specimens used in the estimation of material parameters for Type 2 Diatomite. Specimens used for the uniaxial strain and conventional triaxial compression tests at 50, 600 and 1000 psi were prepared from preserved cores. Specimens used for the conventional triaxial compression tests at 100 and 300 psi were prepared from

unpreserved cores. Tests Lhls_13Ab (50 psi) and Lhls_16b (100 psi) clearly reached a peak stress difference, and failure in Lhls_14b (300 psi) was imminent. However, data from the two unpreserved specimens conflicted with the other test data and was not used in estimation of the shear failure parameters (recall that the Type 2 diatomite has the highest clay content of the three types). Also, for physically realistic parameter estimation it was necessary to constrain the difference A-C to be positive, and the shear failure parameters were estimated from the data at 50, 600 and 1000 psi. Figure 4.5 shows the model fit to the triaxial data along with the shear failure parameters. The cap plasticity parameters were determined using the two uniaxial strain tests and the triaxial compression tests at 50, 300, and 600 psi. The test at 1000 psi was not included because of the large hold time that followed hydrostatic load-up that precluded estimation of cap hardening. Figure 4.6 shows the model fit to these data along with the best-fit parameters.

Table 4.4 Type 2 Diatomite test information and derived elastic properties

Test No.	Sample ID	Depth (ft.)	Bulk Density (g/cm^3)	Load Path	2x Shear Modulus (psi)	Bulk Modulus (psi)
Lhls_13ab	13-3A	1,656.6	1.560	Triaxial Compression (50 psi)	No unload	No unload
Lhls_16b	16-1C	1,666.0	1.531	Triaxial Compression (100 psi)	No unload	No unload
Lhls_14b	14-1B	1,664.8	1.633	Triaxial Compression (300 psi)	116,375	84,655
Lhls_11b	11-3A	1,656.6	1.509	Triaxial Compression (600 psi)	No unload	No unload
Lhls_9b	9-3A	1,656.6	1.468	Triaxial Compression (1000 psi)	78,592	Undefined (E=120,367)
Chv1a-1	1A1	1,655.6	1.681	Uniaxial Strain	92,000	68,518
Chv1a-1g	1A2	1,655.6	1.659	Uniaxial Strain	118,377	87,068

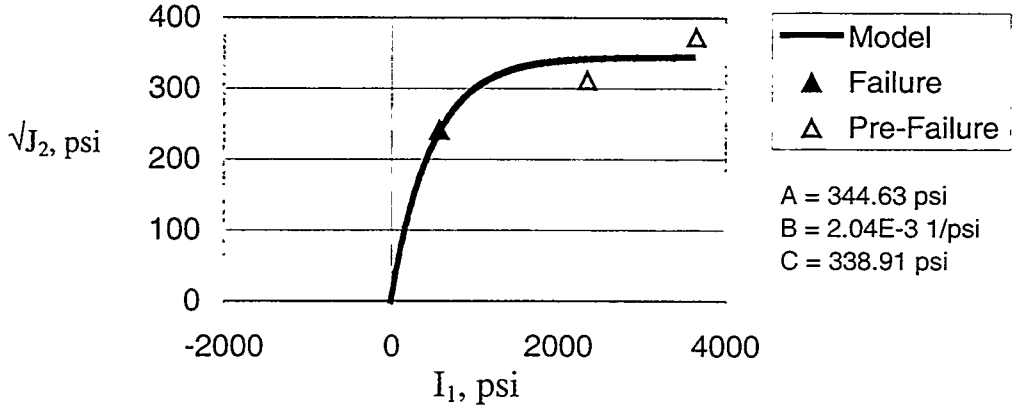

Figure 4.5 Shear failure model fit to conventional triaxial compression test data for Type 2 Diatomite (see Table 4.4)

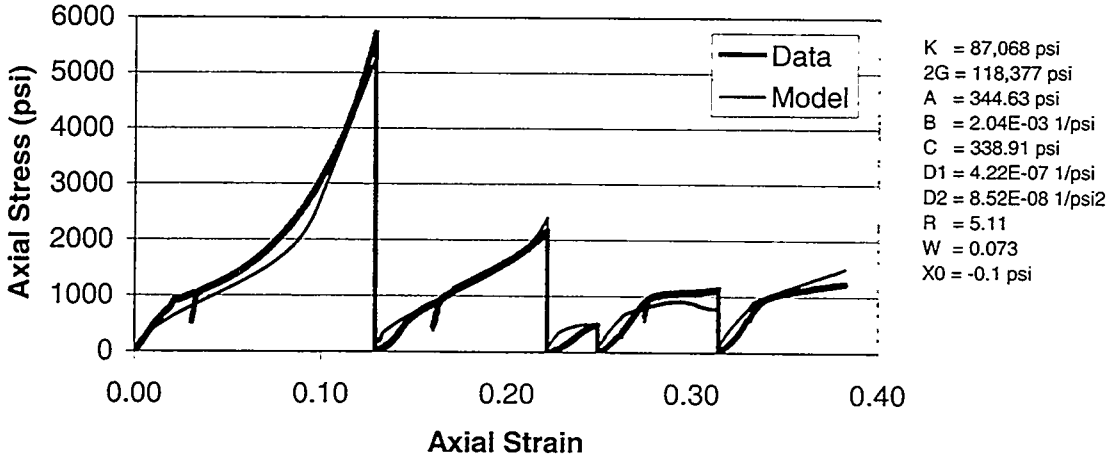

Figure 4.6 Measured versus predicted axial stress – axial strain behavior for two uniaxial strain tests (first two tests shown) and three triaxial compression tests at 50, 300, and 600 psi (third through fifth shown) for Type 2 Diatomite (see Table 4.4). Note that the hydrostatic load segments of the triaxial tests are included. Inclusion of the test at 300 psi did not affect the cap parameter optimization.

4.4.4 Etchegoin Formation – C Sand

Only conventional triaxial compression load paths were available to derive cap parameters for the reservoir sands of the Etchegoin Formation (C and D sands). Because none of the principal strains are controlled under the conventional triaxial compression load path, the parameter optimization in the absence of uniaixal strain data was more complicated.

Table 4.5 identifies the specimens used in the estimation of material parameters for the Etchegoin C Sand. All specimens were unpreserved. Tests Aera_1hb (unconfined), Aera_1ib (100 psi), and Aera_1lb (300 psi) reached a peak stress difference, while tests Aera_1kb (600 psi) and Aera_1mb (1000 psi) did not reach a peak stress difference. In order to constrain the shear failure surface at higher mean stress, it was necessary to estimate the hardening behavior and extrapolate the stress-strain behavior to approximate the shear stress at failure for the test at 1000 psi. Figure 4.7 shows the model fit to the shear failure data along with the values of the shear failure parameters. Only the axial stress – strain data of the triaxial compression test at 600 psi (Aera_1kb) was used for determination of the cap plasticity model parameters. The tests at 100, 300 and 1000 psi included protracted hold periods that precluded use of that data because of the time independence of the material model. "Zeroing out" the strains during the hold period is not possible because commensurate with the strains during the hold period is cap hardening. The cap hardening affects the cap behavior upon resumption of the triaxial loading and therefore the hold period cannot be simply zeroed out. Inclusion of the unconfined test caused the parameter optimization to be problematic, possibly because of the very small radial strains measured in that test. Figure 4.8 shows the model fit to this test along with the values of the best-fit parameters.

Table 4.5 Etchegoin C Sand test information and derived elastic properties

Test No.	Sample ID	Depth (ft.)	Bulk Density (g/cm^3)	Load Path	2x Shear Modulus (psi)	Bulk Modulus (psi)
Aera_1hb	1H	1,498.8	1.728	Uniaxial Compression	No Unload	No Unload
Aera_1ib	1I	1,498.1	1.728	Triaxial Compression (100 psi)	No Unload	No Unload
Aera_1lb	1L	1,498.1	1.728	Triaxial Compression (300 psi)	69,764	67,650
Aera_1kb	1K	1,498.1	1.728	Triaxial Compression (600 psi)	No Unload	No Unload
Aera_1mb	1M	1,498.1	1.728	Triaxial Compression (1000 psi)	118,218	Undefined (E=177,911)

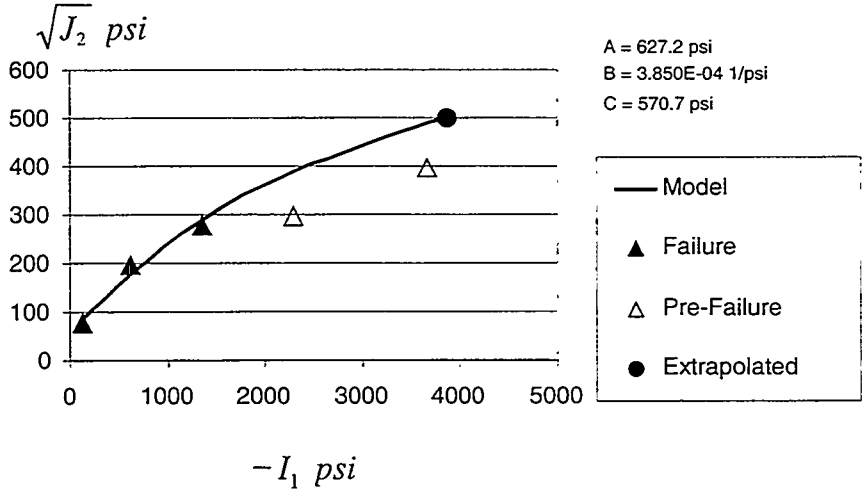

Figure 4.7 Shear failure model fit to conventional triaxial compresison test data for Etchegoin Sand C (see Table 4.5)

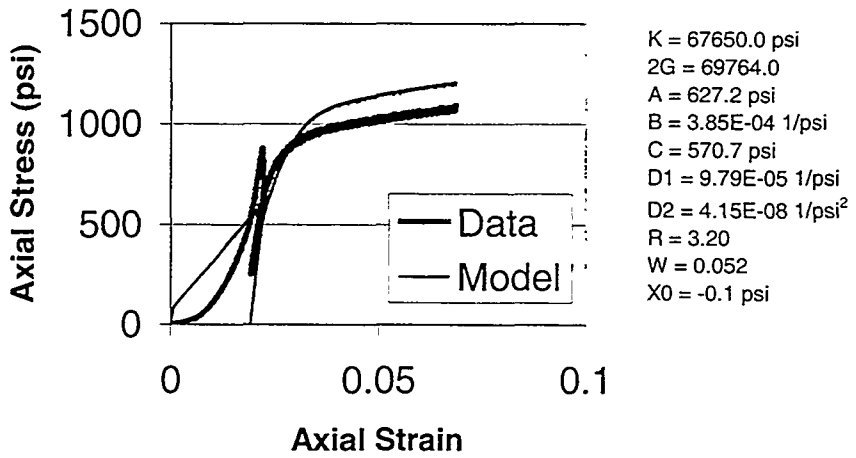

Figure 4.8 Measured versus predicted axial stress – axial strain behavior for the triaxial compression tests for Etchegoin Sand C at a confining pressure of 600 psi. Note that the hydrostatic load segment is included (also see the stress overload that occurred inadvertently during the hydrostatic portion).

4.4.5 Etchegoin Formation – D Sand

Table 4.6 identifies the specimens used in the estimation of material parameters for the Etchegoin D Sand. All test specimens were unpreserved. Tests Aera_2gb (unconfined), Aera_2hb (100 psi), and Aera_2ib (300 psi) reached a peak stress difference, while tests Aera_2jb and Aera_2kb (600 and 1000 psi) did not. As described previously, the hardening behavior during the test at 1000 psi was estimated to allow approximation of the failure stress at elevated mean stresses. Figure 4.9 shows the model fit to the shear failure data along with the values of the shear failure parameters. The axial stress-strain data of all five triaxial compression tests were used in simulation of the cap model parameters. Figure 4.10 shows the model fit to these tests along with the values of the best-fit parameters.

Table 4.6 Etchegoin D Sand test information and derived elastic properties

Test No.	Sample ID	Depth (ft.)	Bulk Density (g/cm^3)	Load Path	2x Shear Modulus (psi)	Bulk Modulus (psi)
Aera_2gb	2G	1,627.6	1.712	Uniaxial Compression	No Unload	No Unload
Aera_2hb	2H	1,627.6	1.712	Triaxial Compression (100 psi)	No Unload	No Unload
Aera_2ib	2I	1,627.6	1.712	Triaxial Compression (300 psi)	87,102	84,581
Aera_2jb	2J	1,627.6	1.712	Triaxial Compression (600 psi)	No Unload	No Unload
Aera_2kb	2K	1,627.6	1.712	Triaxial Compression (1000 psi)	133,850	224,533

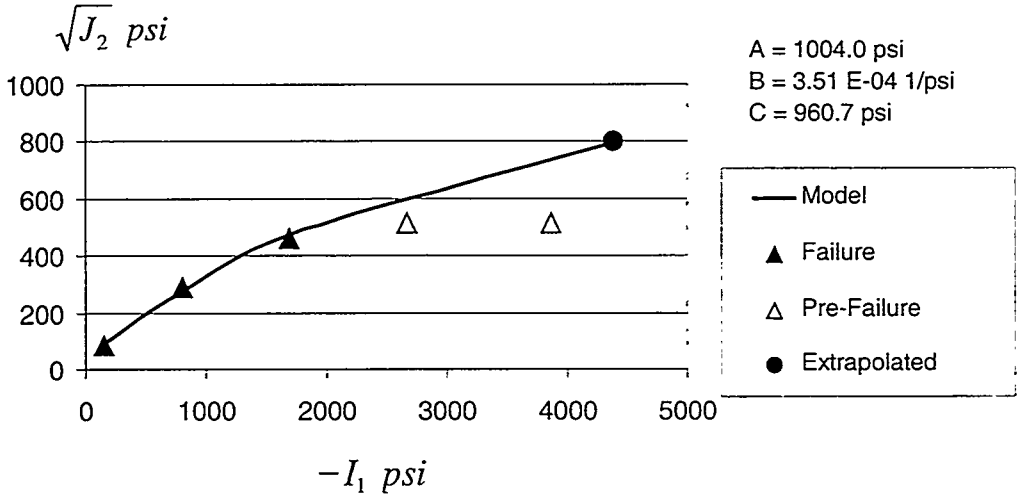

Figure 4.9 Shear failure model fit to conventional triaxial compresison test data for Etchegoin Sand D (see Table 4.7)

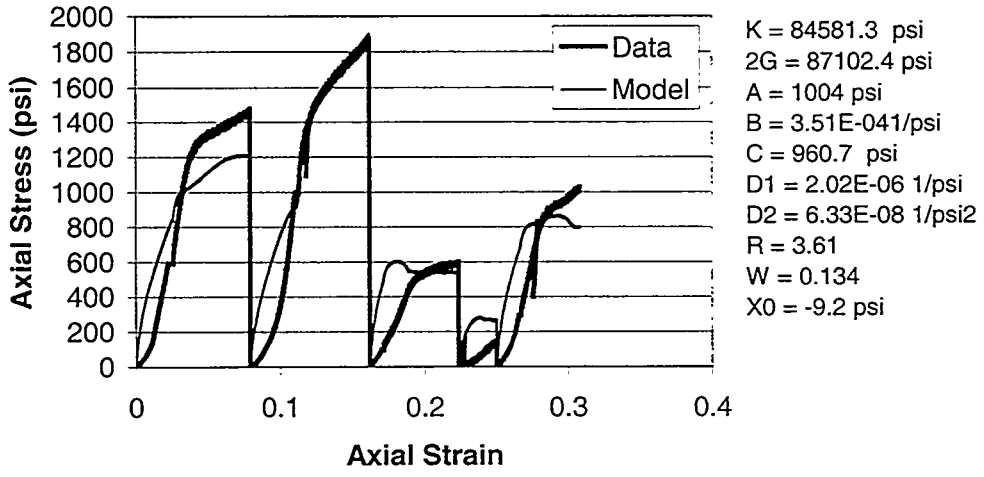

Figure 4.10 Measured versus predicted axial stress – axial strain behavior for five triaxial compression tests for Etchegoin Sand D (see Table 4.7). Note that the hydrostatic load segments of the triaxial tests are included.

4.4.6 Etchegoin Formation – Belridge Diatomite Interface (D Sand / E Cycle)

A core was also provided from the approximate location of the interface between the Etchegoin Formation and Belridge Diatomite Unit. Table 4.7 identifies the specimens used in the estimation of material parameters for the D/E interface material. Tests Aera_3bb (unconfined), Aera_3cb (100 psi), and Aera_3db (300 psi), reached a peak stress difference, and Aera_3eb (600 psi) appeared to be close to peak stress. The test Aera_3fb (1000 psi) did not, and the hardening behavior was extrapolated as described previously. Figure 4.11 shows the model fit to the shear-failure data along with the values of the shear-failure parameters. Cap parameters were not derived, and this unit was not defined in the geomechanical model.

Table 4.7 Sand D – Cycle E (Interface) test information and derived elastic properties

Test No.	Sample ID	Depth (ft.)	Bulk Density (g/cm^3)	Load Path	2x Shear Modulus (psi)	Bulk Modulus (psi)
Aera_3bb	3B	1,653	1.546	Uniaxial Compression	No Unload	No Unload
Aera_3cb	3C	1,653	1.546	Triaxial Compression (100 psi)	No Unload	No Unload
Aera_3db	3D	1,653	1.546	Triaxial Compression (300 psi)	33,429	38,298
Aera_3eb	3E	1,653	1.546	Triaxial Compression (600 psi)	No Unload	No Unload
Aera_3fb	3F	1,653	1.546	Triaxial Compression (1000 psi)	70,808	197,498

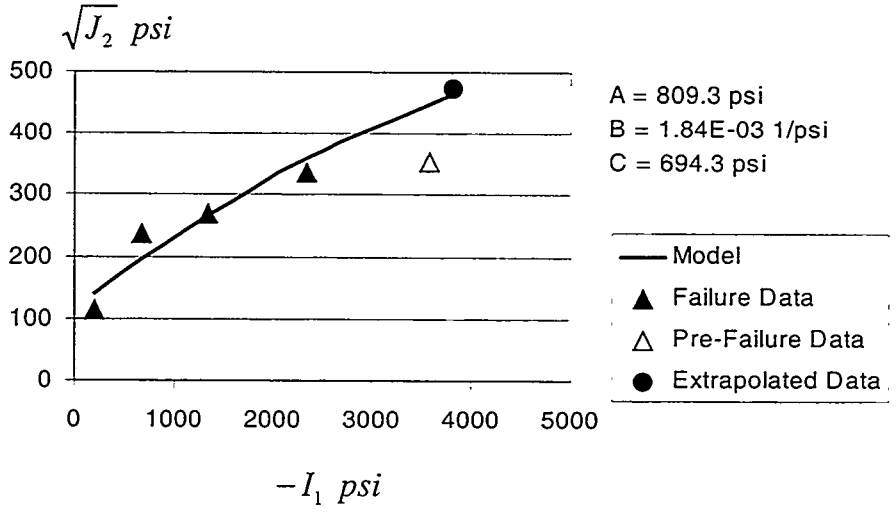

Figure 4.11 Shear failure model fit to conventional triaxial compresison tests for the Etchegoin Formation – Belridge Diatomite interface core (see Table 4.7).

4.4.7 Porcelanite (underburden)

Table 4.8 identifies the specimens used in the estimation of material parameters for the Opal CT phase of the Belridge Diatomite Member. All specimens reached failure. Figure 4.12 shows the model fit to the shear failure data along with the values of the shear failure parameters.

Table 4.8 Belridge Diatomite (Opal CT) test information and derived elastic properties

Test No.	Sample ID	Depth (ft.)	Bulk Density (g/cm^3)	Load Path	2x Shear Modulus (psi)	Bulk Modulus (psi)
Chv31-1b	3-1	2658	1.65	Triaxial Compression (50 psi)	No Unload	No Unload
Chv32-1b	3-2	2658	1.65	Triaxial Compression (100 psi)	No Unload	No Unload
Chv33-1b	3-3	2658	1.65	Triaxial Compression (300 psi)	482,793	274,333
Chv22-1b	2-2	2631	1.65	Triaxial Compression (600 psi)	No Unload	No Unload
Chv23	2-3	2631	1.65	Triaxial Compression (1000 psi)	394,127	234,532

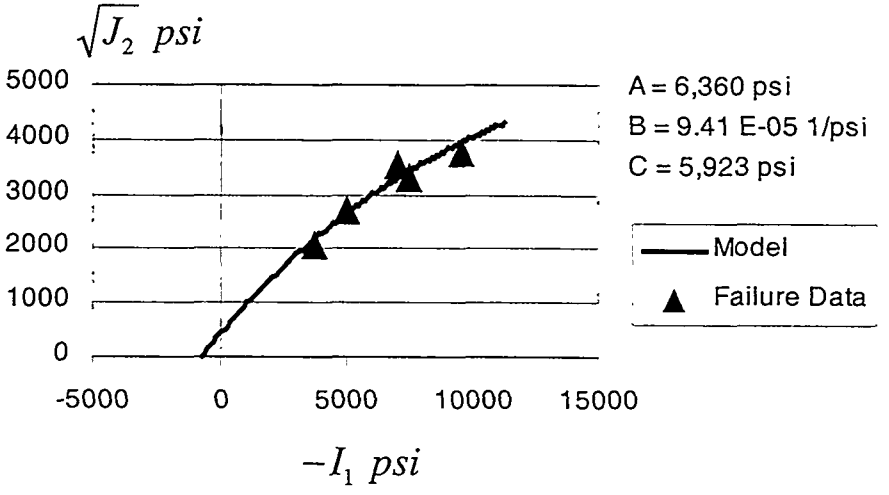

Figure 4.12 Shear failure model fit to conventional triaxial compression tests for the Opal CT phase of the Belridge Diatomite Member, Porcelanite (see Table 4.8)

4.4.8 Overburden Formations

No core was available for material testing for the overburden formations. Material parameters were estimated from the best data available from the literature.

San Joaquin Formation. The elastic properties, K = 93,333 psi and 2G = 74,667 psi, for the San Joaquin siltstone, are from *Bruno and Bovberg* (1992). Shear-failure parameters for the ESR cap model were determined from their Mohr envelope failure data based on rock mechanics tests on cores from the Lost Hills Field. Figure 4.14 shows the model fit to these shear failure data along with the values of the shear failure parameters.

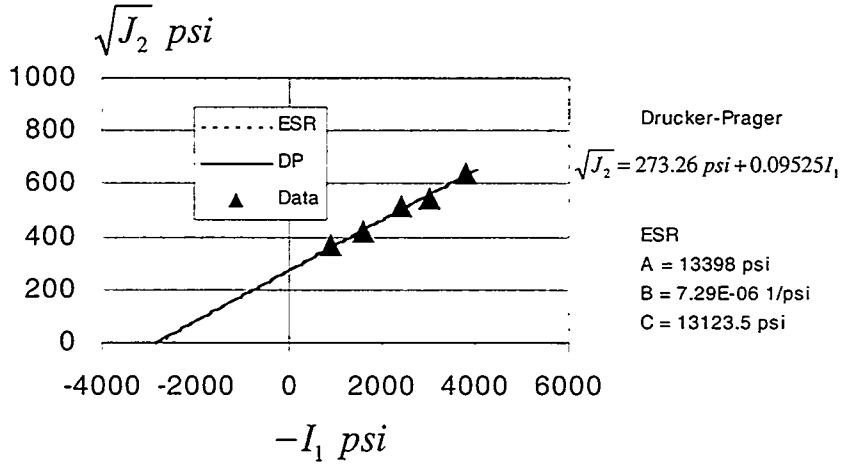

Figure 4.13 Shear failure model fit to shear failure data deduced from Mohr envelope failure data for the San Joaquin Formation reported by *Bruno and Bovberg* (1992)

Tulare Formation. The elastic properties, K = 23,333 psi and 2G = 28,000 psi, for the Tulare Formation at the Belridge Field were as reported in *Fredrich et al.* (1996). Drucker-Prager parameters reported by *Fredrich et al.* (1996) were converted to equivalent shear failure parameters for the ESR cap model. Figure 4.14 shows a comparison of the Drucker-Prager shear failure locus with the equivalent ESR shear failure locus over the stress range of interest.

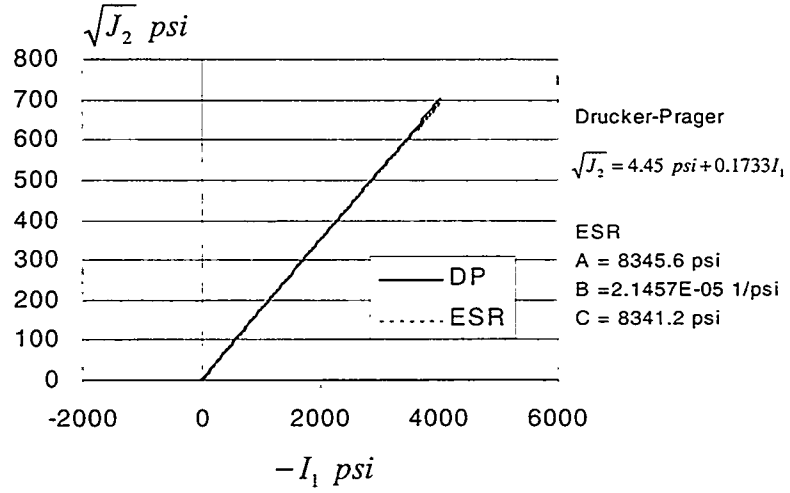

Figure 4.14 Comparison of the Drucker-Prager shear failure locus with the equivalent ESR shear-failure locus for the Tulare Formation (based on constitutive model parameters from the Belridge Field as reported in *Fredrich et al.* (1996)

Alluvium. The elastic properties, K = 15,000 and $2G$ = 13,846 psi, for the alluvium at the Belridge Field, were as reported by *Fredrich et al.* (1996). The Drucker-Prager

parameters presented in *Fredrich et al.* (1996) were converted to equivalent shear failure parameters for the ESR cap model. Figure 4.15 shows a comparison of the Drucker-Prager shear-failure locus with the equivalent ESR shear failure locus over the stress range of interest.

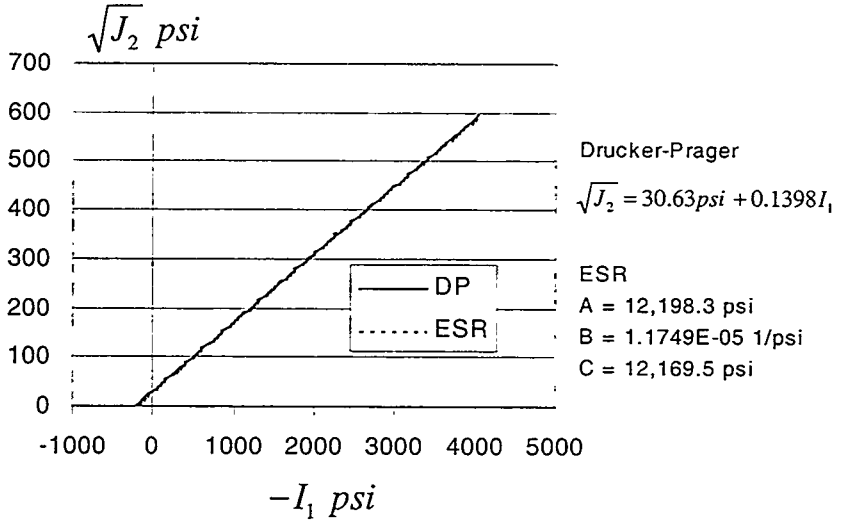

Figure 4.15 Comparison of the Drucker-Prager shear failure locus with the equivalent ESR shear failure locus for alluvium at the Belridge Field

5 Discussion

5.1 Summary and Comparison of Constitutive Models

Table 5.1 summarizes the material models developed for the overburden, underburden, and reservoir formations at the Lost Hills oil field. As described previously, the diatomite reservoir is varied vertically in composition due to its cyclic sedimentary origin. This work follows the convention of the two field operators who define three type diatomites that are delineated based on bulk density and composition.

Table 5.1 Material Parameters for the Etchegoin Sands, Belridge Diatomite, and Overburden Formations at the Lost Hills Oil Field, California

Material Parameter	alluvium	Tulare Formation	SJ Formation	Etchegoin C Sand	Formation D Sand	D/E Interface	Belridge Diatomite Type 1	Type 3	Type 2	Opal CT
K (psi)	15,000	23,333	93,333	67,650	84,581	38,297	44,031	77,745	87068	274,333
2G (psi)	13,846	28,000	74,667	69,764	87,102	33,429	64,399	99,707	118,377	482,792
ρ (g/cu cm)				1.73	1.71	1.55	1.58	1.73	1.57	1.65
A (psi)	8,345.60	12,198.30	13,398.00	627.2	1,004	809.3	442.61	449.85	344.63	
B (1/psi)	2.15E-05	1.18E-05	7.29E-06	3.85E-04	3.51E-04	1.84E-03	1.22E-03	1.39E-03	2.04E-03	9.41E-05
C (psi)	8,341.20	12,169.50	13,123.50	570.7	960.7	694.3	422.65	440.19	338.91	5923.4
D 1 (1/psi)	•	•	•	9.79E-05	2.02E-06	•	9.79E-05	7.00E-07	4.22E-07	•
D2 (1/psi2)	•	•	•	4.15E-08	6.33E-08	•	4.15E-08	6.32E-08	8.52E-08	•
R	•	•	•	3.2	3.61	•	3.204	2.34	5.11	•
W	•	•	•	0.052	0.134	•	0.1288	0.12	0.073	•
X0 (psi)	•	•	•	-0.1	-9.2	•	-0.1	-0.1	-0.1	•

To complement the parameter listing in Table 5.1, the relative mechanical behavior of the three type diatomites is illustrated from a physical perspective in Figures 5.1 through 5.3. These figures show the material models and cap hardening behavior for the three type diatomites in mean – deviatoric stress space (I_1 vs $\sqrt{J_2}$) . The cap yield surfaces plotted represent the cap positions at plastic volume strains of 1, 3, 6, and 10%. In cases where the maximum compaction strain that the model predicts (that reflects the laboratory experiments) is less than 10%, the cap position at that strain is shown instead. Thus, the shape and position of the cap for the different diatomite types illustrate their relative compactability and compaction hardening behavior.

The shear yield surfaces for the Type 1 and 3 diatomites are similar, and both are stronger than the Type 2 diatomite. However, the cap behavior for Types 1 and 3 differs slightly, with different cap curvature, and with Type 3 being somewhat more compaction-resistant (i.e., the cap hardens more than it does for Type 1). More importantly, note that the elastic properties of the Type 1 and 3 diatomites are significantly different, with close to a factor of 2 difference in the bulk modulus of the Type 1 versus Type 3 diatomite. Therefore, it is essential to distinguish between the two material models for Type 1 and 3. As noted, the Type 2 diatomite is the weakest in regard to shear failure. The cap hardening behavior for the Type 2 diatomite is also markedly different, such that the cap hardens dramatically at volume strains greater than ~5% as compared to the hardening behavior of Types 1 and 3.

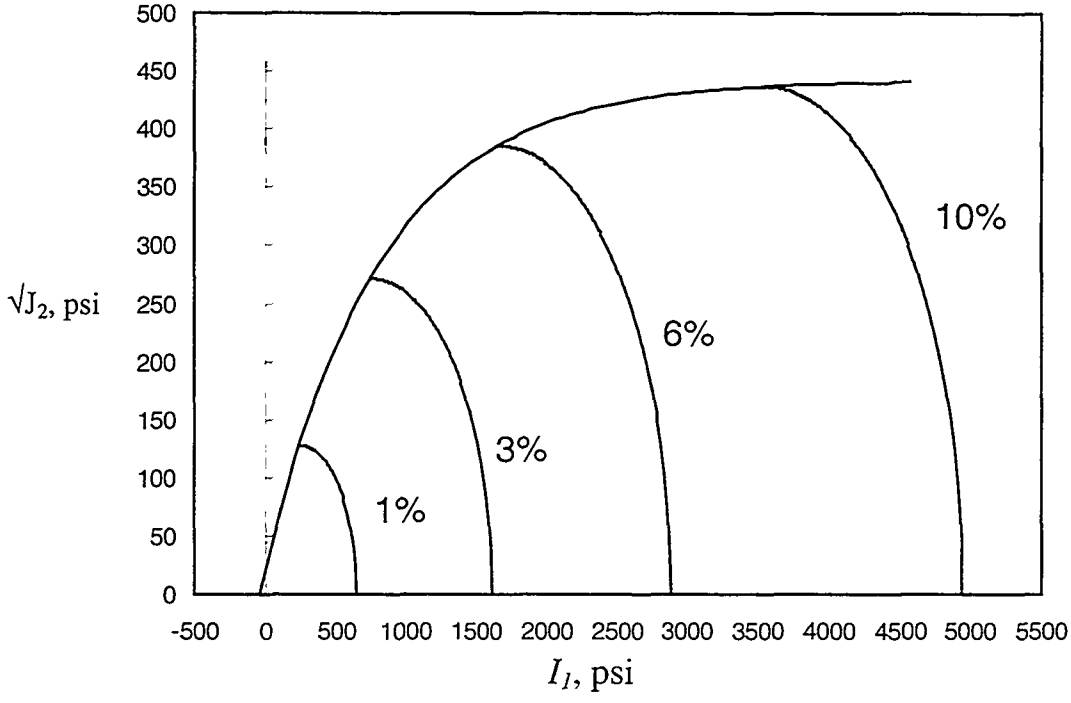

Figure 5.1 Cap plasticity model for the Type 1 Diatomite. The cap hardening behavior is illustrated by the isovolume cap surfaces at plastic strains of 1, 3, 6, and 10%

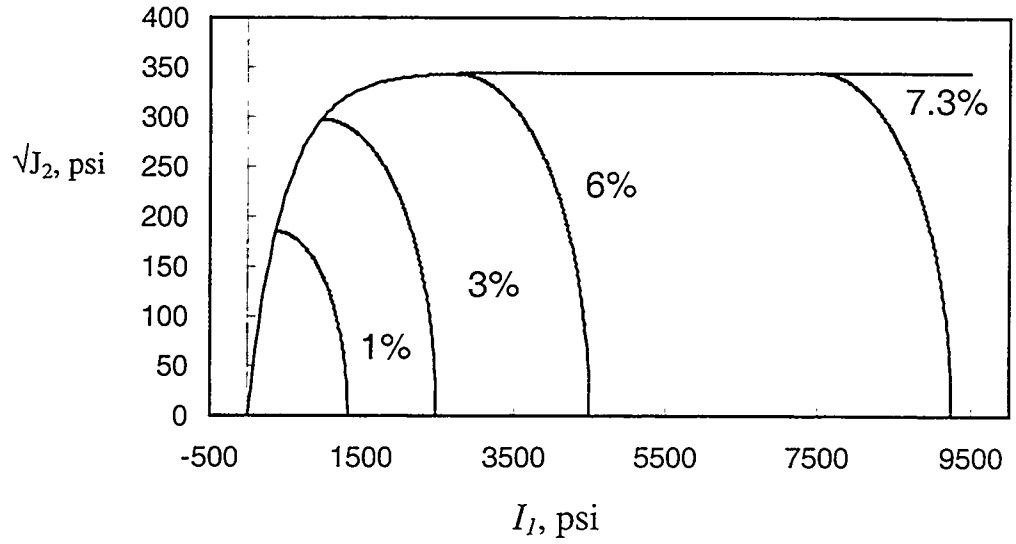

Figure 5.2 Cap plasticity model for the Type 2 Diatomite. The cap-hardening behavior is illustrated by the isovolume cap surfaces at plastic strains of 1, 3, 6, and 7.3%

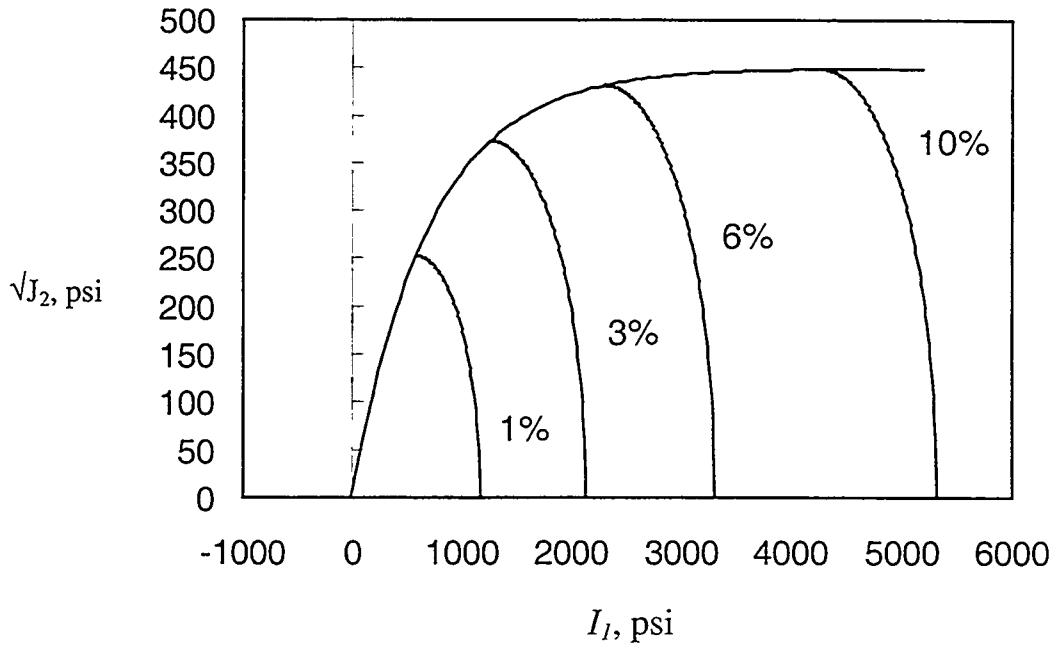

Figure 5.3 Cap plasticity model for the Type 3 Diatomite. The cap-hardening behavior is illustrated by the isovolume cap surfaces at plastic strains of 1, 3, 6, and 10%

The cap plasticity models for the Etchegoin reservoir formations, Sands C and D, are shown in Figures 5.4 and 5.5. Sands C and D are significantly stronger than the three type diatomites of the Belridge Diatomite unit. Also, the C Sand compaction-hardens more than the D Sand, and the yield surfaces are less sensitive to shear stress.

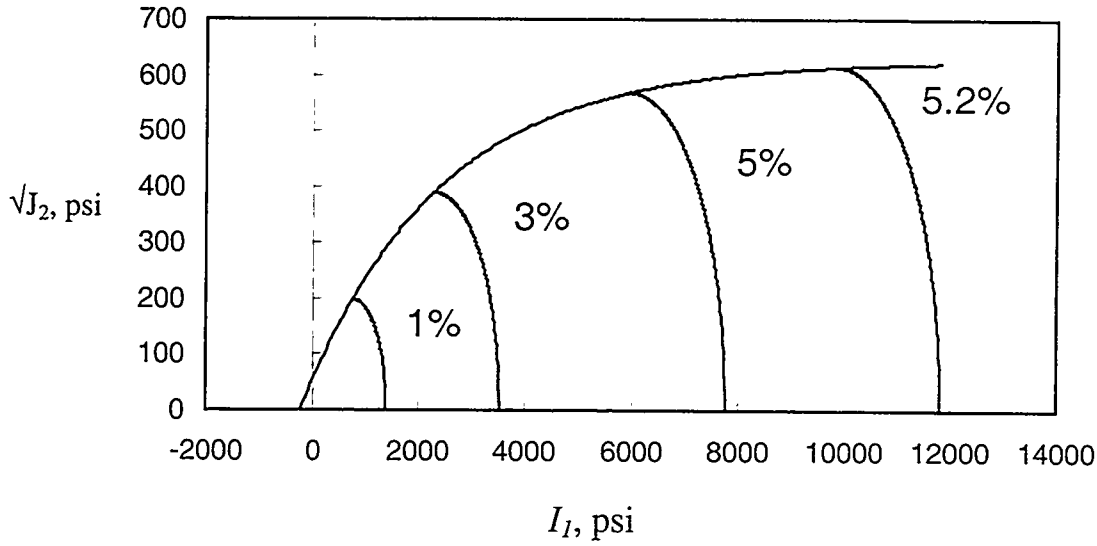

Figure 5.4 Cap plasticity model for the Etchegoin C sand. The cap hardening behavior is illustrated by the isovolume cap surfaces at plastic strains of 1, 3, 5, and 5.2%.

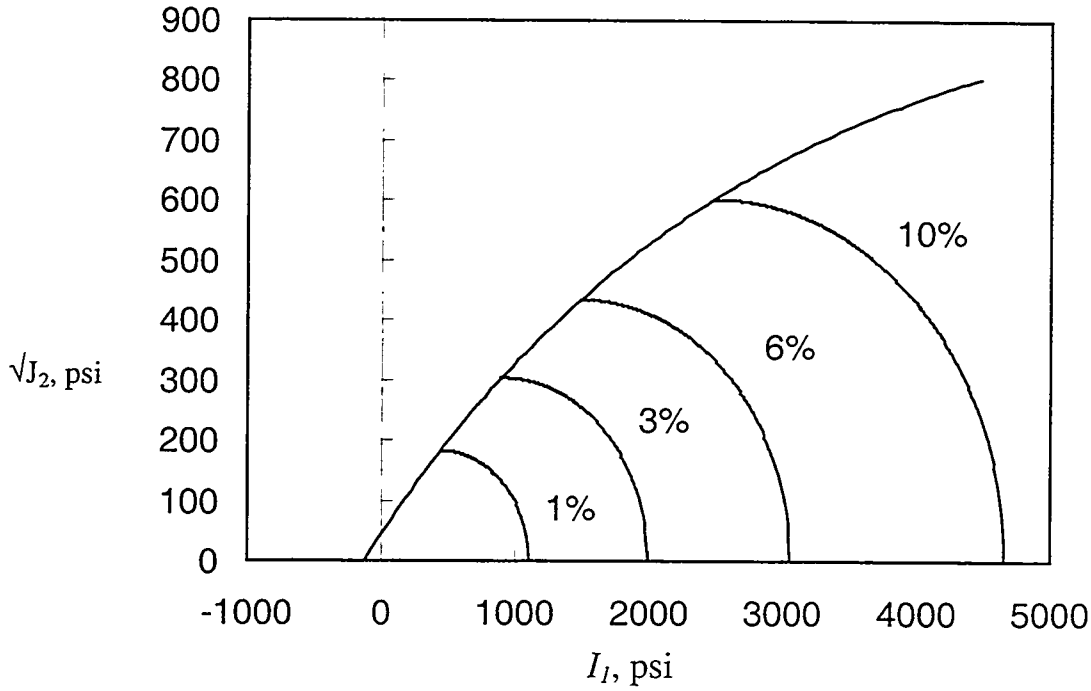

Figure 5.5 Cap plasticity model for the Etchegoin C sand. The cap hardening behavior is illustrated by the isovolume cap surfaces at plastic strains of 1, 3, 6, and 10%

5.2 Other Issues

The laboratory rock mechanics experiments indicate that all of the rocks tested are somewhat anisotropic. That is, under a hydrostatic loading path in which all of the principal stresses are maintained equal, the radial and axial strains differ. Typically, the sample is more compliant in the vertical direction, and the material is probably transversely isotropic, with the axis of rotational symmetry oriented vertically (i.e., perpendicular to bedding). It should be noted that the material model applied here assumes isotropy, and therefore does not capture this aspect of the material deformation. At the present time, only an isotropic cap plasticity model is implemented in JAS3D.

A second feature of the rock mechanics behavior that the present material model does not capture is the transition from compactive to dilatant deformation that generally precedes shear failure. *Fossum and Fredrich* (2000) describe the application of a newly-developed continuous-surface cap plasticity model to this data, and show that the new model represents the actual behavior more accurately than the traditional cap plasticity model used here that precludes the occurrence of dilatant deformation at stress states below the shear failure surface. This behavior is only realized at stress states very close to the intersection of the cap yield and shear failure surfaces, and so this aspect is not relevant for stress states sufficiently removed from the shear failure surface.

5.3 Geomechanical Model of Lost Hills

The material models were developed for use in three-dimensional geomechanical simulations of the Lost Hills field that will be described in detail in a future report by Fredrich et al. In brief, the 3D geomechanical model was meshed so as to include parts of Sections 4, 5, 32, and 33, and included wells operated by both Chevron USA Prod. Co. and Aera Energy LLC. The model was meshed directly from marker data provided by Chevron USA Prod. Co with the layers in the geomechanical model being defined by the marker data. Assignment of type diatomite models to layers in the geomechanical model was based on analyses of lithologic correlation sections that were developed from neutron density well log data for approximately 20 wells that transected the reservoir structure at Lost Hills. The lithologic correlation sections included some wells in the area of the geomechanical model and were provided by Chevron USA Prod. Co. Contact surfaces were also included at specific horizons based on analyses of the field well failure data. The essential features of the geomechanical model are summarized in Figure 5.6.

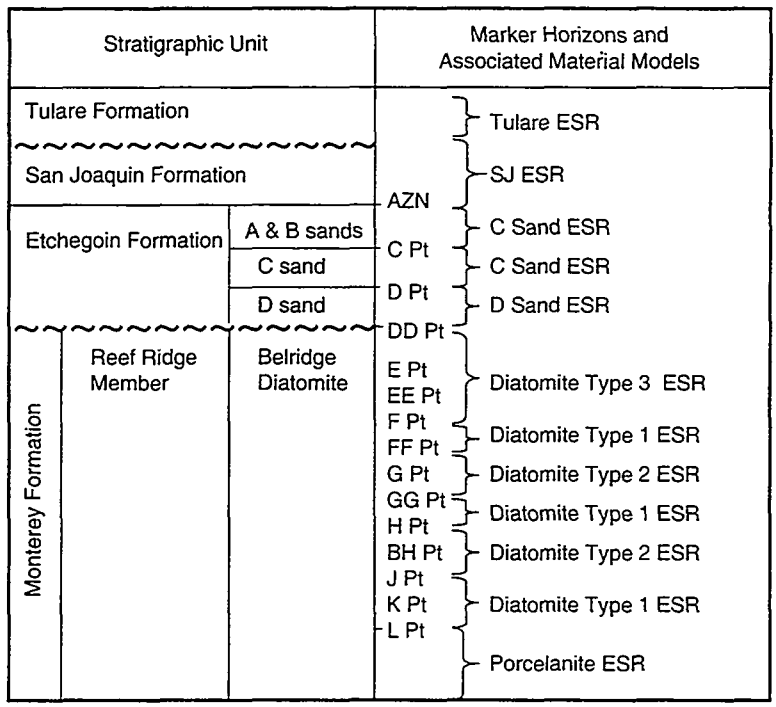

Figure 5.6 Schematic illlustrating the correlation of constitutive models with marker horizons used to mesh the 3D geomechanical model of the Lost Hills Field. The geomechanical model also includes two contact surfaces located at the AZN and F points. The reservoir horizon is shown with gray shading for clarity. Note that there is no vertical scale.

6 Summary

Constitutive models were developed for the reservoir formations, overburden formations, and underlying strata at the Lost Hills oil field, Kern County, California. Parameters for an Extended Sandler-Rubin (ESR) cap plasticity model were derived for the two reservoir formations, and shear failure parameters of the ESR cap model were determined for both overburden and underburden formations.

Our work followed the convention of the two field operators who define three type diatomites that are delineated based on bulk density and composition. The analyses of the rock mechanics experiments indicated that the three type diatomites have distinct differences in their mechanical behavior. The failure strengths of Type 1 and 3 Diatomites are similar; however, their elastic properties differ substantially. Also, Type 3 is slightly more compaction-resistant than Type 1. The Type 2 Diatomite is the weakest in regard to shear failure, and the cap behavior is also markedly different, and exhibits rapid hardening at relatively modest plastic volume strains. Table 5.1 and Figure 5.6 summarize the material models and geomechanical layer definitions that were developed in this work.

It is emphasized that the constitutive models developed here are valid only within the ranges of stress and strain of the laboratory data from which they are derived. In particular, it is noted that the position of the shear failure surfaces at higher mean stresses would be better constrained in the presence of additional laboratory data that included triaxial compression tests that were extended to shear failure.

The material models developed here are presently being used in three dimensional geomechanical simulations of the Lost Hills field that will be described in a future report. The geomechanical model includes parts of Sections 4, 5, 32, and 33, and includes wells operated by Chevron USA Prod. Co. and Aera Energy LLC.

7 References

Blanford, M. L. et al., JAS3D– A multi-strategy iterative code for solid mechanics analysis, Users' Instructions, Release 1.4, Internal Memorandum, Sandia National Laboratories, Albuquerque, New Mexico, 1996.

Bruno, M.S. and C. A. Bovberg, "Reservoir compaction and surface subsidence above the Lost Hills Field, California," *Proc. 33rd US Symp. on Rock Mechanics*, AA Balkema, Rotterdam, p. 263-272, 1992.

Fast, R. E., A. S. Murer, and R. S. Timmer, "Description and analysis of cored hydraulic fractures, Lost Hills Field, Kern County, California," SPE 24853, *Proc. 67th Annual Technical Conference and Exhibition*, Society of Petroleum Engineers, Washington DC, October 4-7, 1992.

Fast, R. E., A. S. Murer, and L. G. Zambrano, "Lost Hills diatomite simulation study: Predicting waterflood performance in a low-permeability, compacting reservoir," SPE 26627, *Proc. 68th Annual Technical Conference and Exhibition*, Society of Petroleum Engineers, Houston TX, October 3-6, 1993.

Fossum, A. F., "Parameter estimation for an internal variable model using nonlinear optimization and analytical/numerical response sensitivities," *J. Eng. Mat. and Tech.*, 119, 337-345, 1997.

Fossum, A. F. and J. T. Fredrich, "Estimation of constitutive parameters for the Belridge Diatomite, South Belridge Diatomite Field," SAND98-1407, Sandia National Laboratories, Albuquerque, New Mexico, 1998.

Fossum, A. F. and J. T. Fredrich, "Cap plasticity models and dilatant and compactive pre-failure deformation," *Proc. 4th North American Rock Mechanics Symp.*, Seattle, WA, July 31-August 3, 2000, A.A. Balkema, Rotterdam (in press).

Fossum, A. F., et al., "Continuous, three-invariant, single-surface dilation/compaction plasticity model with mixed hardening and limit-state weakening," in preparation, 2000.

Fredrich, J. T., J. G. Arguello, B. J. Thorne, W.R. Wawersik, G. L. Deitrick, E.P. de Rouffignac, L. R. Myer, and M. S. Bruno, "Three-dimensional geomechanical simulation of reservoir compaction and implications for well failures in the Belridge diatomite," SPE 36698, *Proc. 71st Annual Technical Conference and Exhibition*, Society of Petroleum Engineers, Denver CO, October 6-10, 1996.

Fredrich, J. T., G. L. Deitrick, J. G. Arguello, & E. P. deRouffignac, "Reservoir compaction, surface subsidence, and casing damage: A geomechanics approach to mitigation and reservoir management," in *Eurock- Rock Mechanics in Petroleum Engineering*, p. 403-412, SPE/ISRM 47284, Society of Petroleum Engineers, 1998.

Fredrich, J. T., G. L. Deitrick, J. G. Arguello, & E. P. deRouffignac, "Geomechanical modeling of reservoir compaction, surface subsidence, and casing damage at the Belridge diatomite field," accepted for publication in *SPE Reser. Eval. and Eng.*, 2000.

Graham, S. A., and L. A. Williams, "Tectonic, depositional, and diagenetic history of Monterey Formation (Miocene), central San Joaquin basin, California," *AAPG Bull.*, 69, 385-411, 1985.

Myer, L., J. Jacobsen, J. Horsman, J.T. Fredrich, W.R. Wawersik, J.G. Arguello, M. Bruno, and H. Qian, "Use of visualization techniques in analysis of well failures in diatomite reservoirs," *The Leading Edge*, 185-189, March 1996.

Sandler, I. S. and D. Rubin, An algorithm and a modular subroutine for the cap model, *Int. J. Num. Anal. Meth. Geomech.*, 3, 173-186, 1979.

Stewart, M., D. Stewart, and M. Gaona, "Fracturing alliance improves profitability of Lost Hills field," *Oil & Gas J.*, 83-89, Nov. 1994.

External Distribution:

Aera Energy LLC (4)
5060 California Ave.
P.O. Box 11164
Bakersfield, CA 93389-1164
Bob Gwinn
Dave Mayer
Tom Moroney
Tony Murer

Chevron Petroleum Technology Co. (2)
P.O. Box 6019
San Ramon, CA 94583
Russ Ewy
Greg Mazmanian

Chevron Research & Technology Co. (1)
100 Chevron Way
Richmond, CA 94802
Craig Bovberg

Chevron USA Prod. Co. (4)
4900 California Ave.
Bakersfield, CA 93309
Dave Shephard (3)
Jerry Cales (1)

Shell E&P Tech. Co. (2)
BTC 1136
P.O. Box 481
Houston, TX 77001
Greg Deitrick
Eric de Rouffignac

Chuck Dobie
Crutcher-Tufts Prod. Co.
5500 Ming Ave., Suite 210
Bakerfield, CA 93309

Bob Shore
Bakersfield Energy Resources
2131 Mars Court
Bakersfield, CA 93308

Kalon Degenhardt
Texaco Exploration and Production Inc.
Box 519TX
Bakersfield, CA 93308

Larry Myer
Lawrence Berkeley Laboratory
Earth Sciences Division, MS 50C
Berkeley CA 94720

Mike Bruno
Terralog Technologies
332 E. Foothill Blvd, Suite B
Arcadia CA 91006

U.S. Department of Energy (2)
National Petroleum Technology Office
P.O. Box 3628
Tulsa, OK 74101
Bob Lemmon
Jerry Casteel

Ahmed Abou-Sayed
Advantek International
3300 S. Gessner Road
Suite 257
Houston, TX 77063

Maurice Boutéca
Institut Francais du Petrole
1 et 4, avenue de Bois-Preau
92852 Rueil-Malmaison Cedex
France

Professor Robert Charlier
Universite de Liege
MSM- Institut du Génie Civil
Quai Banning, 6-B-4000 Liège
Belgium

Nigel Higgs
Higgs Technologies, LLC
Mansion House, Suite 1120
1638 South Carson Street
Tulsa, OK 74119

Professor J. Casey Moore
Earth Sciences
University of California
Santa Cruz, CA 95064

David Parrish
CenterLine Consulting
Professional Offices
P.O. Box 330
Rapid City, South Dakota 57709

Tom Pfeifle
RE/SPEC Inc.
P.O. Box 725
Rapid City, SD 57709

Professor Rasmus Risnes
Stavanger College
P.O. Box 2557 Ullandhaug
N-4004 Stavanger, Norway

Professor John Rudnicki
Dept. of Civil Engineering
Northwestern University
Evanston IL 60208-3109

Peter M. T. M. Schutjens
Sintef Petroleum Research
SP Andersenvei 15B
7465 Trondheim, Norway

Paul Senseny
Factory Mutual Research
1151 Boston-Providence Turnpike
Norwood, MA 02062-9102

Steve Willson
BP Amoco Corp.
501 WestLake Park Blvd.
Houston, TX 77079-2696

Exxon Prod. Res. Co. (2)
David Yale
David Olgaard
P.O. Box 2189
Houston, TX 77252-2189

TerraTek Inc. (2)
Roberto Suarez
John McLennan
420 Wakara Way
Salt Lake City, UT 84108

Internal Distribution:

MS0750 6116 File (5)
MS0750 D. J. Borns, 6116
MS0750 J. T. Fredrich, 6116 (15)
MS0750 J. C. Lorenz, 6116
MS0750 S. E. Minkoff, 6116
MS0750 M. C. Walck, 6116
MS0750 N. R. Warpinski, 6116
MS0751 M.Y. Lee, 6117
MS0751 W.A. Olsson, 6117
MS0751 D.H. Zeuch, 6117
MS0751 L. S. Costin, 6117
MS0701 P. B. Davies, 6100
MS0741 S. G. Varnado, 6200
MS9405 R. A. Regueiro, 8726
MS0834 M. R. Baer, 9100
MS0828 T. C. Bickel, 9101
MS0834 A. C. Ratzel, 9112
MS0847 C. M. Stone, 9121
MS0835 J. S. Peery, 9121
MS0847 A. F. Fossum, 9123 (5)
MS0847 H. S. Morgan, 9123
MS0847 W. M. Scherzinger, 9123
MS0847 J. G. Arguello, 9126
MS0847 J. F. Holland, 9126
MS0847 R. A. May, 9126
MS0847 B. J. Thorne, 9126
MS0828 J. L. Moya, 9132
MS0303 T. Warren, 15414
MS0303 M. J. Forrestal, 15414
MS9018 Central Technical Files, 8940
MS0899 Technical Library, 9616 (2)
MS0612 Review and Approval Desk, 9612
for DOE/OSTI